



HAL
open science

Homo-heterojunction concept: From simulations to high efficiency solar cell demonstration

Tristan Carrere, Raphaël Lachaume, Quang Minh Thai, Marianne Coig,
Jean-Paul Kleider, Delfina Munoz

► To cite this version:

Tristan Carrere, Raphaël Lachaume, Quang Minh Thai, Marianne Coig, Jean-Paul Kleider, et al.. Homo-heterojunction concept: From simulations to high efficiency solar cell demonstration. Solar Energy Materials and Solar Cells, 2018, 182, pp.178 - 187. 10.1016/j.solmat.2018.03.027 . hal-01808875

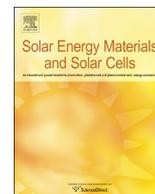
HAL Id: hal-01808875

<https://centralesupelec.hal.science/hal-01808875>

Submitted on 30 Mar 2020

HAL is a multi-disciplinary open access archive for the deposit and dissemination of scientific research documents, whether they are published or not. The documents may come from teaching and research institutions in France or abroad, or from public or private research centers.

L'archive ouverte pluridisciplinaire **HAL**, est destinée au dépôt et à la diffusion de documents scientifiques de niveau recherche, publiés ou non, émanant des établissements d'enseignement et de recherche français ou étrangers, des laboratoires publics ou privés.



Homo-heterojunction concept: From simulations to high efficiency solar cell demonstration

Tristan Carrere^{a,b,c}, Raphaël Lachaume^b, Quang Minh Thai^b, Marianne Coig^d, Jean-Paul Kleider^b, Delfina Munoz^{a,*}

^a CEA-INES, LITEN, Laboratoire HET, 50 Avenue du Lac Léman, 73375 Le Bourget-du-Lac, France

^b GeePs, UMR8507 CNRS, Centrale Supélec, Université Paris-Sud, Sorbonne Universités UPMC Univ Paris 6, 11 rue Joliot Curie, 91192 Gif-sur-Yvette cedex, France

^c French Environment and Energy Management Agency, 20 avenue du Grésillé BP 90406, 49004 Angers cedex 01, France

^d CEA-LETI, MINATEC Campus, 17 rue des Martyrs, 38054 Grenoble, France

ARTICLE INFO

Keywords:

Heterojunction solar cells
Boron implantation

ABSTRACT

The novel solar cell architecture called silicon homo-heterojunction (HHJ) cell is investigated combining experimental and simulation approaches. This structure intends to overcome the limitations of the silicon heterojunction technology regarding the amorphous/crystalline silicon interface (*p*) a-Si:H/(*i*) a-Si:H/(*n*) c-Si by the addition of a (*p*⁺) c-Si layer at the hetero-interface. First, the added (*p*⁺) c-Si layer is experimentally investigated using boron implantation through the realization and characterization of symmetric solar cell precursors. An adapted process flow taking into account the (*p*⁺) c-Si profile optimization, the annealing effects on substrate degradation, and the impact on surface passivation, is deeply explored. Then, large area solar cells are processed and the solar cell performance are discussed in view of the data obtained on precursors and with the help of realistic numerical simulations. Overall, we observe that the HHJ solar cells exhibit a small performance improvement compared to reference heterojunction cells. In particular, a gain in the fill factor is observed, which is shown to be originated from both an improvement in field effect and a decrease of the vertical series resistance from the a-Si:H layers. The experimental data obtained on the processed homo-heterojunction solar cells confirm that this technology can lead to improved conversion efficiencies compared to the high quality reference heterojunction solar cells.

1. Introduction

Amorphous/crystalline silicon (a-Si:H/c-Si) heterojunction solar cells (SHJ) have already demonstrated to be a promising alternative to standard homojunction solar cells in terms of efficiency but also in terms of industrial production and cost [1,2]. In 2012, numerous laboratories and companies have strongly improved efficiencies and succeeded obtaining n-type SHJ solar cells with power conversion efficiencies above 21% [3–7]. Moreover, results obtained in 2015 and 2016 by Kaneka surpassed the world record for crystalline silicon solar cells with more than 25% conversion efficiency (25.1% [8] and 26.7% [9,10] on large area regular and back contacted SHJ cells configurations, respectively) confirming the high potential of such structures for high efficiency cells and modules. The key of the SHJ technology is a simple and low temperature (< 200 °C) process based on the deposition of a-Si:H layers onto a c-Si wafer used both to passivate the surface and to build the front junction and back surface field allowing for extremely high V_{OC} [11].

However, in today's SHJ solar cells, the a-Si:H/c-Si interface passivation on the emitter side is identified as one of the most important issue [12,13] limiting the SHJ cells performance specially because of the fill factor (FF)/open-circuit voltage (V_{OC}) compromise. Indeed, the passivation of the surface (limiting the device V_{OC}) is strongly enhanced by the use of an intrinsic (*i*) a-Si:H layer. However, such layer is resistive and impacts negatively the fill factor (FF) increasing vertical series resistances when increasing the thickness, while also impacting the short circuit current due to parasitic absorption, especially in the front emitter configuration. Thus, the (*i*) and (*p*) a-Si:H layer thicknesses are optimized for the compromise between passivation (low interface defect density D_{it}), doping (strong field effect) and vertical conduction. Additionally, the role of the transparent conductive oxide (TCO) [14,15] is required to collect laterally the charges (to insure low lateral series resistances) and to achieve an effective Metal/TCO/(*i/p*) a-Si:H/c-Si contact (correlated to vertical series resistance) [16].

Different approaches have been proposed to improve the passivation/field effect compromise, for instance, improving cleaning [13],

* Corresponding author.

E-mail address: delfina.munoz@cea.fr (D. Munoz).

tuning the (*i*) a-Si:H layers structures and properties [17,18] or band management modifications using silicon based amorphous alloys [19–22].

An alternative option to improve the field effect is by the addition of a thin and highly doped (p^+) c-Si region underneath the (*i*) a-Si:H passivation layer modifying the crystalline silicon space charge region. The resulting structure is called a homo-heterojunction (HHJ) for it combines a homojunction profile to improve band bending and vertical carrier collection with the amorphous hetero-emitter.

In previous numerical simulation studies [23], it was shown that, compared to the SHJ cell, the HHJ cell exhibits a higher open-circuit voltage and is less sensitive to interface defects. These features have been evidenced to originate from the additional field effect passivation brought by the (p^+) c-Si region. Additionally, the HHJ cell fill factor is also improved and less influenced by interface defects [23]. Such improvements were also observed by simulations by other authors on similar homo-heterojunction cells with insertion of a highly doped crystalline layer at the emitter of either n-type or p-type silicon solar cells [24,25].

Concerning experimental results, the HHJ cells fabricated so far did not succeed to surpass the performance of SHJ cells because of their lower V_{OC} due to increased recombination after the (p^+) c-Si processing [26,27]. Such increased recombination could take place in the strongly doped (p^+) c-Si region or could originate from a low (p^+) c-Si/(*i*) a-Si:H chemical passivation. They can also appear in the substrate due to the creation of additional defects related to the high temperature needed for the (p^+) c-Si layer processing (epitaxy, post-implantation annealing or diffusion) [28].

In this work, we use boron implantation to produce the (p^+) c-Si layer. In a first part, ion implantation parameters are optimized using effective lifetime measurements on symmetrical (p^+) c-Si/(*n*) c-Si/(p^+) c-Si samples. Then, in a second part we fabricate HHJ cells and standard SHJ cells. For the first time we were able to obtain HHJ cells exhibiting slightly improved conversion efficiencies compared to the SHJ ones. Results are discussed and explained in the light of further numerical simulations.

2. Experimental details

2.1 Symmetrical p^+np^+ samples

Symmetrical (p^+) c-Si/(*n*) c-Si/(p^+) c-Si samples (p^+np^+) are first processed by implanting boron (B) with a beam-line Varian VIISta® HCP implanter in 160–180 μm thick n-type textured Cz pseudo-square $156 \times 156 \text{ cm}^2$ c-Si substrates with initial resistivity ranging from 3.0 to 4.0 $\Omega \text{ cm}$. Various energies and doses have been tested to obtain different profiles. In particular, c-Si wafers have been taken from the second quarter of the Cz ingot to avoid strong oxygen and metallic impurities known to be detrimental for substrate lifetime when high temperature steps are used during processing [29]. After an HF- O_3 cleaning step, boron is activated around 950 $^\circ\text{C}$ during 15 min in a nitrogen atmosphere. Such low activation temperature has been chosen following a previous work in order to limit bulk substrate damages [28]. By comparing the secondary ion mass spectroscopy (SIMS) results (Fig. 1) with that of electrochemical capacitance-voltage (ECV) (not shown here), the boron atoms were checked to be fully active [30]. Implantation parameters, boron dose and boron surface concentration deduced from SIMS are summarized in Table 1 for five batches (HHJ₁–HHJ₅), each batch consisting in three wafers.

Subsequent to the annealing step at 950 $^\circ\text{C}$, (p^+) c-Si surfaces are passivated using different stacks and layers:

- a 8/72 nm-thick $\text{AlO}_x/\text{SiN}_x:\text{H}$ stack, deposited by atomic layer deposition (ALD) in a Beneq equipment at room temperature and high temperature plasma enhanced chemical vapor deposition (PECVD) in a Centrotherm tool at 450 $^\circ\text{C}$, respectively,

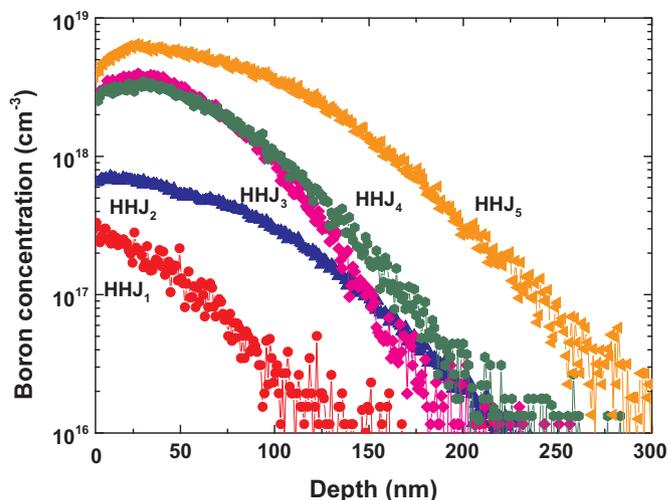


Fig. 1. SIMS measurement of the studied boron implantation profiles, on polished n-type c-Si substrates.

Table 1

Summary of implantation energy and dose conditions tested in this work, with measured boron dose and surface concentration from SIMS measurements after the annealing and the surface cleaning steps, and the corresponding calculated sheet resistance. These values are valid for polished n-type substrates. For textured substrates the implantation dose is multiplied by 1.7 in order to obtain similar sheet resistance from the implanted doped region.

Batch name	Implantation energy kV	Implanted B dose cm^{-2}	Measured B dose cm^{-2}	$[\text{B}]_{\text{surface}}$ cm^{-3}	R_{sh} (Calculated from SIMS) Ω / \square
HHJ ₁	1	1.0×10^{13}	1.7×10^{12}	4.0×10^{17}	1.4×10^4
HHJ ₂	10	1.0×10^{13}	1.0×10^{13}	7.5×10^{17}	4.2×10^3
HHJ ₃	1	1.0×10^{14}	3.1×10^{13}	3.0×10^{18}	1.7×10^3
HHJ ₄	5	5.0×10^{13}	3.0×10^{13}	3.0×10^{18}	1.7×10^3
HHJ ₅	10	1.0×10^{14}	7.3×10^{13}	5.0×10^{18}	8.5×10^2

– a-Si:H layers deposited at 200 $^\circ\text{C}$ by PECVD in a Jusung cluster tool :

- o a $18 \pm 1 \text{ nm}$ thick (*i*) a-Si:H layer,
- o a $20 \pm 1 \text{ nm}$ thick (*i/p*) a-Si:H stack,

It is already known that thanks to the AlO_x negative charges, the $\text{AlO}_x/\text{SiN}_x:\text{H}$ stack passivates very efficiently B-doped c-Si surfaces [31] and will serve as our passivation reference. The (*i/p*) a-Si:H stack is the same as used in SHJ solar cells at INES [8] and will be used for the realization of HHJ cells.

For comparison purposes, we also processed two other batches of symmetrical structures, that we designate as SHJ_{REF} and SHJ_{950 $^\circ\text{C}$} in the following. These are reference samples without any boron implantation and using the standard cleaning procedure developed at INES for the fabrication of silicon heterojunction solar cells [8], except that SHJ_{950 $^\circ\text{C}$} has been submitted to the same annealing step at 950 $^\circ\text{C}$ as the HHJs samples (before deposition of the surface passivation layers) in order to investigate the effect of such annealing on the wafer properties.

Injection dependent effective minority carrier lifetime curves are obtained using a WCT-120 Sinton Instrument setup. For an easy and rapid comparison these curves can be used to extract the effective lifetime at an injection level of 10^{15} cm^{-3} [32] or the implied open-circuit voltage ($i\text{-}V_{OC}$) [33].

For samples with the (*i/p*) a-Si:H passivation stack, we also deposited top co-planar electrodes made of a bi-layer of indium tin oxide (ITO) covered with silver, with various interspacing distances. We applied the transfer length method (TLM) in order to get insight into



Fig. 2. Sketch of the HHJ solar cell in the rear emitter configuration.

conduction properties [34,35].

From the SIMS profiles of Fig. 1 we calculated the implanted boron dose and compared it to the nominal dose (see Table 1). One can note that the two values are not identical, the measured dose being lower than the nominal one. This difference can originate from matrix atoms sputtering due to ion implantation or from the surface etching due to post-implantation and post-annealing cleaning routines [36].

2.2 Solar cells fabrication

Large area (on 156 mm pseudo square wafers) SHJ and HHJ solar cells are processed in a rear emitter configuration (see Fig. 2) at INES pilot line “Labfab” [37] with an industrial process. To finish the solar cell, after the amorphous layers processing, ITO is deposited by PVD on both sides using masks covering the edges to avoid parasitic shunt resistances. Then, solar cells are screen printed with a 4 bus bars bifacial configuration. Solar cells are characterized using IV measurements under 1-sun AM1.5 illumination conditions with an Aescusoft solar simulator. In order to get further insight into the new cell features, Suns- V_{OC} [38] and photoluminescence (PL) [39] measurements are also performed. Series resistances are extracted from the comparison between IV and SunsVoc as suggested by [40].

3. Results and discussions

3.1 a-Si:H passivation on boron-doped surfaces

First, the amorphous silicon passivation quality on the (p^+) c-Si layer needs to be evaluated. We aim at obtaining passivations of the new hetero-interface of at least similar quality as for standard SHJ cells. This is required in order to benefit from the (p^+) c-Si layer addition in terms of collection while guaranteeing high V_{OC} . The effective lifetime as a function of excess carrier density of p^+np^+ samples is plotted in Fig. 3 for each passivation system and for the five implantation conditions and the two reference samples.

In Fig. 3a, effective lifetime curves of HHJ samples passivated by the $AlO_x/SiN_x:H$ system are found close to those of the reference samples.

The difference between samples is larger at low injection level, which can be explained by a difference in field effect whether the $AlO_x/SiN_x:H$ stack is deposited directly onto the n-type c-Si wafer or on the implanted p^+ region. The difference is weaker in the intermediate to high injection level (HIL) range (for excess carrier densities larger than 10^{15} cm^{-3}), where field effect passivation is less prominent. This shows that all implanted (p^+) c-Si bulk regions are lowly defective and do not strongly intrinsically limit the effective lifetime of the samples. Therefore, all tested implantation conditions are potentially suitable for the HHJ application where we can expect high implied- V_{OC} values.

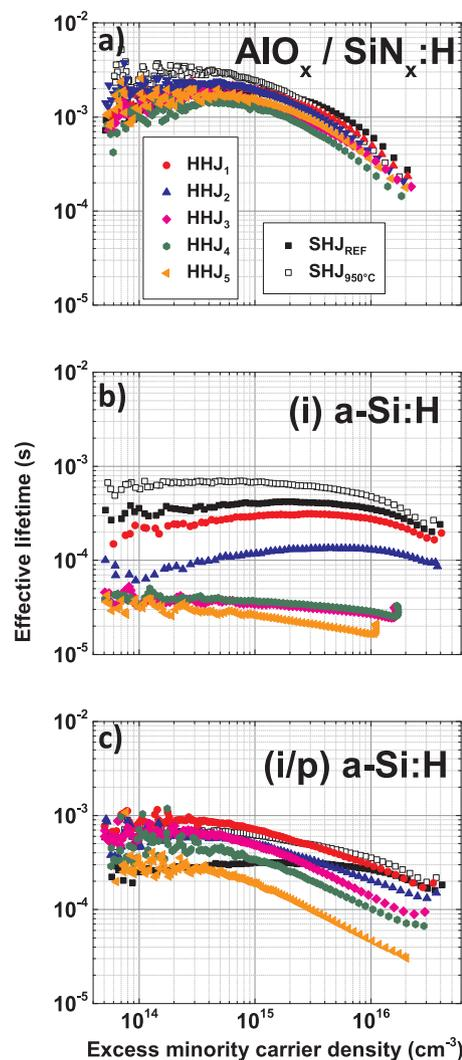


Fig. 3. Effective lifetime as a function of the excess minority carrier density for all symmetric samples with the different B profiles for a) the $AlO_x/SiN_x:H$, b) the (i) a-Si:H and c) the (i/p) a-Si:H passivation stacks.

However, from Fig. 3b, the samples with implanted profiles (HHJ samples) have lower effective lifetimes than both reference samples (SHJ_{REF} , $SHJ_{950^\circ C}$) when passivated by (i) a-Si:H. This decrease is observed on the whole injection level range, meaning that the chemical passivation is decreased for the boron-doped surfaces (i.e. they have higher D_{it}).

Using the (i/p) a-Si:H passivation stack (that is used in heterojunction solar cells) we observe an increase in the effective lifetime at low injection level compared to the samples using only the single (i) a-Si:H passivation layer (Fig. 3c), while the increase at high injection is less pronounced, which is a signature of the field effect passivation [41], indicating that the (p) a-Si:H layer adds a field effect with a significant contribution to the passivation, although less pronounced than the one provided by the $AlO_x/SiN_x:H$ passivation stack. From this figure one can already deduce that HHJ₁ and HHJ₂ exhibit comparable lifetime values at high injection as the SHJ samples and better values at low injection. They are thus expected to improve the solar cells FF and pseudo-FF (pFF) values [42], and will be privileged for the realization of solar cells which results will be described in Section C.

For a better readability and analysis of the lifetime curves at both low and high injection conditions, Fig. 4 summarizes the values of effective lifetime at an excess carrier density of 10^{15} cm^{-3} , τ^{LIL} and the values of implied-open-circuit voltage $i-V_{OC}$, which are representative

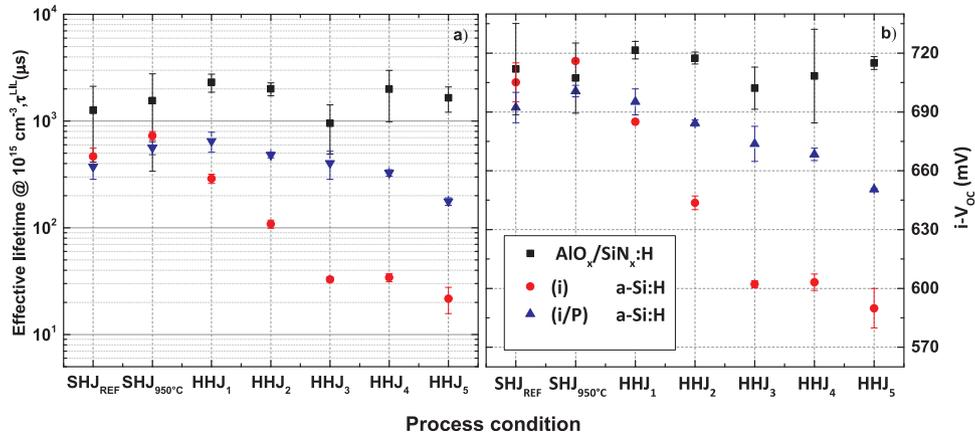


Fig. 4. a) Effective lifetime at excess minority carrier concentration of 10¹⁵ cm⁻³ (low injection level), τ^{LIL}, and b) Implied open-circuit voltage (i-V_{oc}) at 1 sun (high injection level) for different passivation stacks.

of the low and high injection regimes, respectively.

First of all, by comparing the results of SHJ_{REF} and SHJ_{950°C} we note that τ^{LIL} is slightly increased after annealing whatever the passivation system. Such improvement probably originates from oxygen-related phenomena in the c-Si wafer. Dissolution of as-grown thermal donors (TD) upon annealing has been characterized by a resistivity increase from 2.5 to 6 Ωcm, corresponding to an initial TD concentration of 5 × 10¹⁴ cm⁻³. Such phenomenon occurs at temperatures above 600 °C [43] and is known to suppress recombination-active defects [44]. Complementary tests with very high passivation (i)/(n) stack (not shown) demonstrate that TD were shown to limit τ^{LIL} at 2 ms at the concentration of 5 × 10¹⁴ cm⁻³ [45]. Therefore, assuming samples to have the same interface recombination velocities for SHJ_{ref} and SHJ_{950°C}, TD dissolution is likely to explain the effective lifetime increase upon annealing. This also evidences that the bulk lifetime plays a significant role in the device effective lifetime limitation.

Compared to AlO_x/SiN_x:H, the limited a-Si:H passivation on the (p⁺) c-Si surface is a striking result of this experiment. Such effect was previously evidenced for highly doped homo-emitters obtained from homojunction-type boron diffusion with saturation current densities J_{0e} above 100 fAcm⁻² and sheet resistances lower than 200 Ω/□ [46,47].

In our experiments, the boron profiles in the HHJ samples are softer, with J_{0e} values lower than 60 fAcm⁻² for the AlO_x/SiN_x:H passivation stack. Interestingly, in the tested boron surface concentration ([B]^{Surf}) range τ^{LIL} exhibits a linear dependence on [B]^{Surf} in a log-log plot (see Fig. 5: Effective lifetime at excess minority carrier concentration of 10¹⁵ cm⁻³ (low injection level), τ^{LIL}, as a function of the boron surface concentration for the various passivation layers: (i) a-Si: H, (i/p) a-Si: H

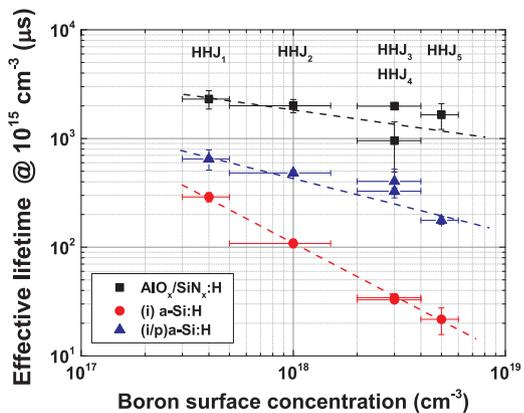


Fig. 5. Effective lifetime at excess minority carrier concentration of 10¹⁵ cm⁻³ (low injection level), τ^{LIL}, as a function of the boron surface concentration for the various passivation layers: (i) a-Si:H, (i/p) a-Si:H and AlO_x/SiN_x:H.

and AlO_x/SiN_x: H.).

To our knowledge no study has so far evidenced such a behavior. This suggests a power law dependence τ^{LIL} ∼ ([B]^{Surf})^γ. While γ is close to zero for the AlO_x/SiN_x:H passivation stack, where field effect passivation can make recombination less sensitive to interface defects and thus to [B]^{Surf}, γ is approximately -0.5 and -1 for the (i/p) a-Si:H and (i) a-Si:H passivation layers, respectively. The latter indicates that interface defect densities increase proportionally to the surface boron concentration and that (i) a-Si:H provides a limited chemical passivation on strongly boron-doped surfaces.

We have evidenced in this first experiment a limited chemical passivation of a-Si:H on strongly boron-doped surfaces. Interestingly, Carstens et al. demonstrated that tuning the (i) a-Si:H deposition and annealing temperature could improve the passivation on boron-doped c-Si surfaces [47]. The passivation level is maximized when a-Si:H is deposited at low temperature. Thus, the involved mechanism seems to be related to as-deposited a-Si:H hydrogen content and H configuration variation from poly-hydride to mono-hydride configurations upon annealing [17]. J_{0e} values as low as 30 fAcm⁻² for 30 nm thick (i) a-Si:H passivation on a stronger diffused homo-emitter (R_□ = 90 Ω/□) have been reported using a 150 °C deposition temperature and post-deposition annealing of 5 min at 350 °C [47]. Additional post-process annealing steps up to 300 °C have been performed on our samples but no effective lifetime increase has been observed. This result is likely to originate from the need of large H content in a-Si:H after deposition in order to enable passivation improvements upon annealing [17]. Thus deposition of a-Si:H at lower temperature could be envisaged in the future for further passivation improvements.

3.2 Effect of the (p⁺) c-Si region in conduction issues

TLM measurements have been performed on samples with the (i/p) a-Si:H stack. From such measurements one can extract a sheet resistance (R_{sh}) [34], that is related to the lateral current flow between the two top electrodes, either in the a-Si:H or in the c-Si regions. When samples have no implanted (p⁺) c-Si region it was shown that the measured sheet resistance reflects conduction in the strong hole inversion layer at the c-Si surface which is caused by the strong band bending implied by the top (i/p) a-Si:H stack [48], while lateral conduction in a-Si:H is negligible due to the low carrier mobility and low effective doping efficiency in this material. When a (p⁺) c-Si region is processed, both the inversion layer and the (p⁺) c-Si region can participate to the measured sheet resistance.

Fig. 6 shows that the sheet resistance is decreased approximately one order of magnitude for HHJ1 and by a factor of about 300 for HHJ2 compared to the reference samples without (p⁺) c-Si region. This proves that insertion of the (p⁺) c-Si region has a strong effect on the

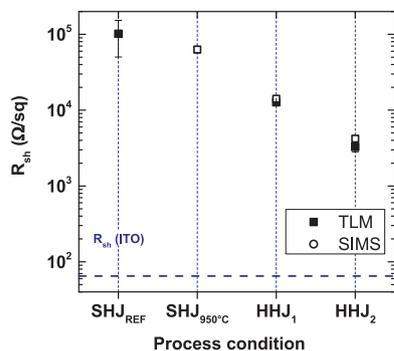


Fig. 6. Measured sheet resistance (R_{sh}), extracted from TLM measurements compared to sheet resistance calculated from SIMS measurement.

band bending and on the Fermi level position at the c-Si surface. Moreover, the R_{sh} values measured from TLM and calculated from SIMS profiles are quite identical. For the latter calculation we first determine the resistivity profile from the measured boron profile (remember that the boron atoms are known to be fully activated from the comparison of ECV and SIMS profiles), with the doping dependent carriers mobility being calculated from the Arora's model [49]. The sheet resistance is then obtained from the reciprocal of the integrated (p^+) c-Si layer conductivity. We however notice that the sheet resistance of the HHJ₂ samples still remains high (by more than one order of magnitude) compared to the ITO sheet resistance, which is at about 65 Ω/\square . Thus no significant lateral current transport improvement is expected in HHJ₁ and HHJ₂ solar cells compared to the reference SHJ cells, and the ITO layer is still mandatory. Only for the strongly implanted HHJ₅ the sheet resistance is decreased to a level of 60 Ω/\square (not shown in this figure) equivalent to that of ITO, but, as mentioned above, such a high implantation level is detrimental regarding passivation issues.

3.3 Solar cells results

Fig. 7: Photovoltaic performance of SHJ and HHJ cells: open-circuit voltage, short circuit current density, fill factor, efficiency, and series resistance. Error bars are standard deviations on at least three samples.

This summarizes the photovoltaic output parameters (open-circuit voltage, short circuit current density, fill factor) of all processed cells and includes the pFF values extracted from Suns- V_{OC} measurements and the calculated series resistances.

HHJ and SHJ cells have similar J_{SC} values (variability is linked to screen printing process). This is consistent with numerical simulations where no short circuit current loss is expected in rear emitter HHJ cells compared to the reference SHJ cells [23].

Open-circuit values of SHJ_{REF}, SHJ_{950°C} and HHJ₁ samples are very similar, meaning that the HHJ₁ cells do not exhibit increased recombination in the homo-emitter and at the hetero-interface. The HHJ₂ cells have a slightly lower V_{OC} because of a lower interface passivation, as observed in the lifetime curves on the symmetrical cell precursors (see Fig. 3b).

The fill factor of HHJ₁ cells is slightly improved, by 0.9% and 0.6% abs. as compared to SHJ_{REF} and SHJ_{950°C} cells, respectively. This FF improvement is explained by both a pFF increase and a series resistance decrease.

To disregard process induced defectivity issues in FF and V_{OC} values, PL images have been performed (Fig. 8).

A striking feature of the figure is that all cells that experienced an annealing step exhibit dark regions principally at the edges due to increased recombination. This originates from the increased number of process steps that implies more samples manipulation and leads to enhanced process induced defectivity. However this is counter balanced by an improved quality of the c-Si material, which was revealed by the measurements on the cell precursors (Fig. 3 et 4). Indeed lifetime

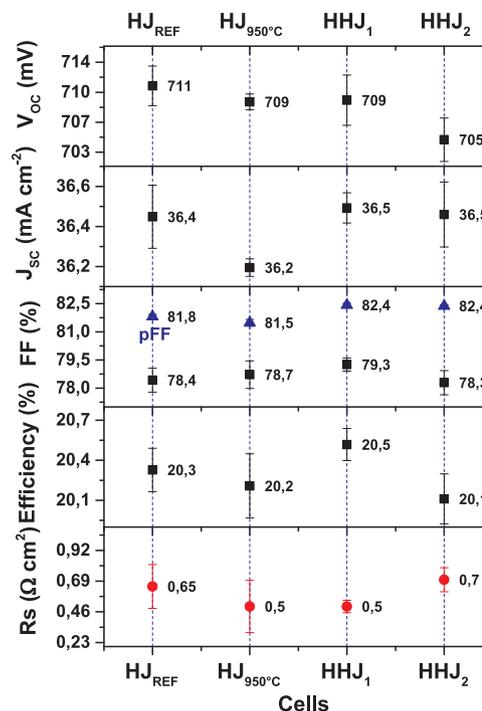


Fig. 7. Photovoltaic performance of SHJ and HHJ cells: open-circuit voltage, short circuit current density, fill factor, efficiency, and series resistance. Error bars are standard deviations on at least three samples.

measurements on the cell precursors are performed in the center of the wafer that is less impacted by sample manipulation. It means that we could reach even higher V_{OC} and FF in the implanted samples if we suppressed the process induced defectivity by improving sample handling.

3.4 General discussion - numerical simulations

In order to gain further insight into the HHJ cells working principle and to discuss experimental results, numerical simulations of both the SHJ and HHJ cells are performed.

3.4.1 Simulation models and parameters

Solar cells simulations are performed using Silvaco Atlas. SHJ cell layer parameters have been taken primarily from Varache's work [50] and have then be adapted in order to closely represent experimental cells as fabricated at INES. They are described in Table 2. The density of states (DOS) in the doped a-Si:H layers follows the defect-pool model proposed by Powell and Deane [51]. For the dangling bonds defects, this leads to Gaussian distributions located at 1.45 eV from the valence band edge (E_V). Because of the statistics for monovalent states used in the modeling, amphoteric dangling bond states are represented as two Gaussian distributions of monovalent states shifted by the correlation energy taken equal to 0.2 eV. Due to the very low thickness of (i) a-Si:H layers, the Fermi level (E_F) position in these layers is much closer from E_V than from the conduction band (E_C). Therefore, according to the defect-pool model the energetic position of localized states originating from dangling bonds is the same as for the doped adjacent layers. However, the absolute values of the Gaussian distributions are taken much lower.

At front and back hetero-interfaces, defects are introduced using a 1 nm thick highly defective c-Si interfacial layer containing two Gaussian distributions of localized states. The donor-like and the acceptor-like Gaussian distributions have their respective maximum at 0.56 eV and 0.76 eV above E_V . Both distributions have a standard deviation of 0.2 eV and electron and holes capture cross sections (σ_e , σ_h)

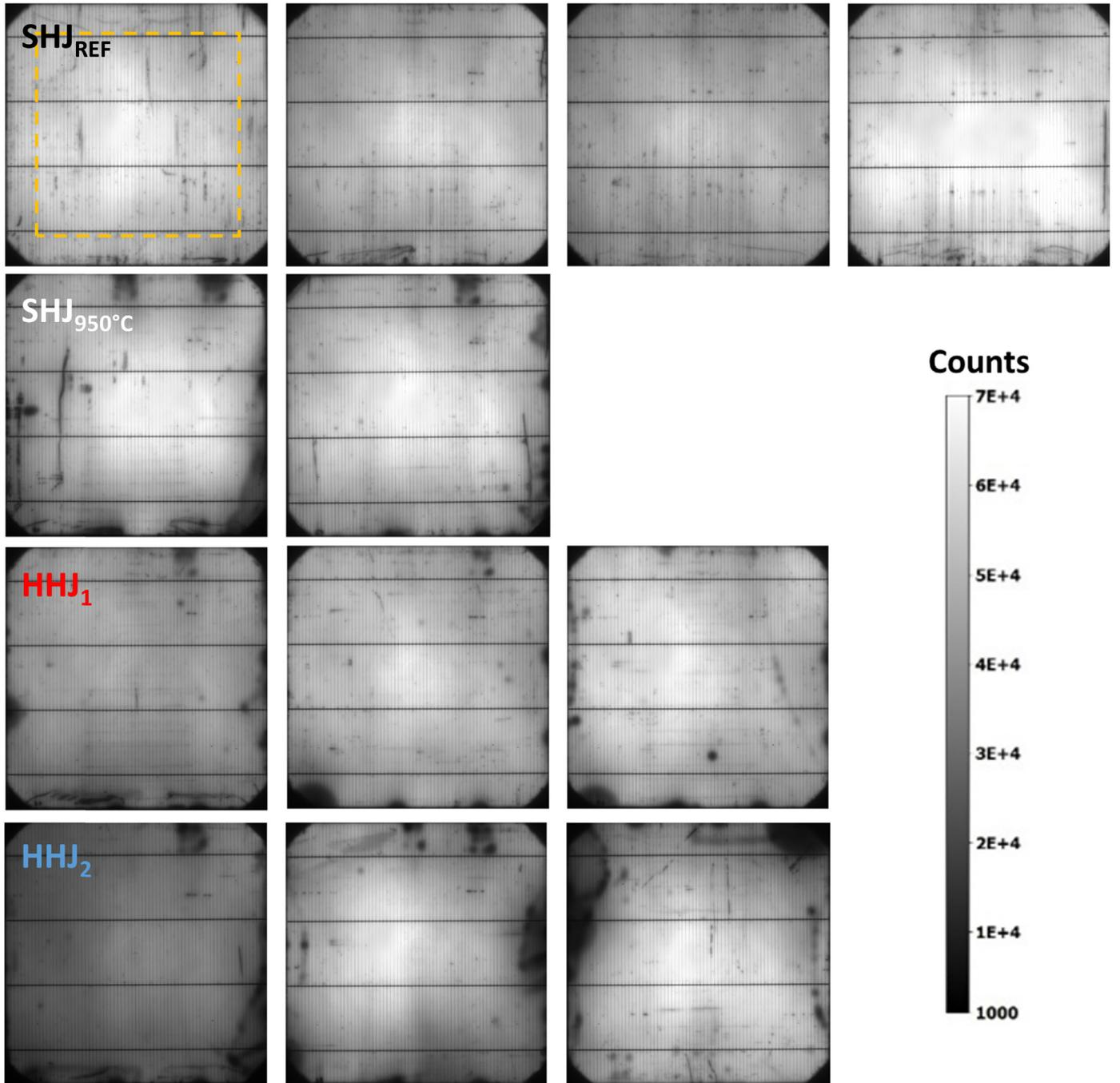


Fig. 8. Photoluminescence images of the processed SHJ and HHJ cells of batch A. The dotted lines represent the active area during the masked IV measurement.

of $1 \times 10^{-14} \text{ cm}^2$. The peak values are adjusted to yield targeted equivalent interface defect densities (D_{it} in cm^{-2}). D_{it} and external resistances were tuned so that the simulated reference SHJ cell displays performances comparable to that of state-of-the-art manufactured cells. D_{it} values are set at 5×10^9 and $1 \times 10^9 \text{ cm}^{-2}$ at the *front* and *back* hetero-interface, respectively. External series resistances are set at $0.5 \Omega \text{ cm}^2$.

In the high quality crystalline substrate (bulk (n) c-Si), recombination centers are modeled with 10^9 cm^{-3} neutral defects located at 0.56 eV above E_V with capture cross sections of 10^{-14} cm^2 .

In the highly doped added layers defects are also located at 0.56 eV above E_V and Shockley-Read-Hall recombination dependence on doping is taken into account in the capture time constant:

$$\tau_{i0high_doping} = \tau_{i0low_doping} * \left(\frac{10^{15}}{N_D} \right)^{0.4}, \quad (1)$$

The lifetime values obtained with this model are below the ones that can be found in literature from other models [52,53]. As a consequence the beneficial effects of the (p^+) c-Si layer insertion will not be over-estimated.

At high dopant densities (i.e. in the added c-Si layers), the band gap narrowing (BGN) effect makes the $p \times n$ product in equilibrium increase above the value that holds at low dopant densities or undoped intrinsic material thus modifying the "intrinsic" carrier concentration following [54] :

$$(n_i^{eff})^2 = N_c N_v * \exp\left(\frac{-(E_g - \Delta E_g^{app})}{kT}\right) = n_i^2 * \exp\left(\frac{\Delta E_g^{app}}{kT}\right), \quad (2)$$

Table 2
Simulated layers parameters. Optical and electrical band gap are considered equal.

Layer parameters	Unit	(p) a-Si:H	(ip) a-Si:H	(n) a-Si:H	(in) a-Si:H	(n) c-Si	(p ⁺) c-Si
Thickness	–	10 nm	3 nm	25 nm	3 nm	149.99 μm	0 – 1000 nm
Band gap	eV	1.700	1.700	1.700	1.700	1.124	1.074 – 1.124
Dopant concentration	cm ⁻³	6.12 × 10 ¹⁹	0	1.71 × 10 ¹⁹	0	2.0 × 10 ¹⁵	1 – 50 × 10 ¹⁷
Relative dielectric constant	–	11.9	11.9	11.9	11.9	11.9	11.9
Electronic affinity	eV	3.824	3.824	3.824	3.824	4.05	4.05
Electron (hole) mobility	cm ² V ⁻¹ s ⁻¹	0.5	0.5	0.5	0.5	1321	225.2 – 1321
		(0.5)	(0.5)	(0.5)	(0.5)	– 461	(96.39 – 461)
Equivalent density in CB (VB)	cm ⁻³	1 × 10 ²⁰	1 × 10 ²⁰	1 × 10 ²⁰	1 × 10 ²⁰	2.843 × 10 ¹⁹	1.08 × 10 ¹⁹
		(1 × 10 ²⁰)	(1 × 10 ²⁰)	(1 × 10 ²⁰)	(1 × 10 ²⁰)	(2.682 × 10 ¹⁹)	(1.019 × 10 ¹⁹)
Neutral defect (at 0.56 eV) concentration	cm ⁻³	–	–	–	–	109	1014
Electron (hole) capture cross section σ _e (σ _h)	cm ²	–	–	–	–	Oct-14	Oct-14
						(10 ⁻¹⁴)	(6.3–30 × 10 ⁻¹⁴)
CB tail (VB tail) density at Ec (Ev)	cm ⁻³ eV ⁻¹	2 × 10 ²²	2 × 10 ²²	2 × 10 ²²	2 × 10 ²²	–	–
		(2 × 10 ²²)	(2 × 10 ²²)	(2 × 10 ²²)	(2 × 10 ²²)		
CB tail (VB tail) Urbach energy	eV	0.035	0.035	0.035	0.035	–	–
		(0.060)	(0.050)	(0.060)	(0.050)		
σ _e and σ _h for CB tail	cm ²	7 × 10 ⁻¹⁶	7 × 10 ⁻¹⁶	7 × 10 ⁻¹⁶	7 × 10 ⁻¹⁶	–	–
σ _e and σ _h for VB tail	cm ²	7 × 10 ⁻¹⁶	7 × 10 ⁻¹⁶	7 × 10 ⁻¹⁶	7 × 10 ⁻¹⁶	–	–
Maximum A- and D-like Gaussian state density	cm ⁻³ eV ⁻¹	1.20 × 10 ²⁰	1.00 × 10 ¹⁷	2.25 × 10 ¹⁹	1.00 × 10 ¹⁷	–	–
Position of the A-(D)-like Gaussian	eV	1.450	1.450	0.850	0.850	–	–
from the valence band edges		(1.250)	(1.250)	(0.650)	(0.650)		
Standard deviation of the A- and D-like Gaussian	eV	0.19	0.19	0.19	0.19	–	–
σ _e (σ _h) for A-like Gaussian states	cm ²	3 × 10 ⁻¹⁵	3 × 10 ⁻¹⁵	3 × 10 ⁻¹⁵	3 × 10 ⁻¹⁵	–	–
		(3 × 10 ⁻¹⁵)	(3 × 10 ⁻¹⁵)	(3 × 10 ⁻¹⁵)	(3 × 10 ⁻¹⁵)		
σ _e (σ _h) for D-like Gaussian states	cm ²	3 × 10 ⁻¹⁵	3 × 10 ⁻¹⁵	3 × 10 ⁻¹⁵	3 × 10 ⁻¹⁵	–	–
		(3 × 10 ⁻¹⁵)	(3 × 10 ⁻¹⁵)	(3 × 10 ⁻¹⁵)	(3 × 10 ⁻¹⁵)		

with n_i^{eff} the equilibrium intrinsic carrier concentration at high doping level, n_i the equilibrium intrinsic carrier concentration without band gap narrowing effect (i.e. at low doping level), N_c (N_v) the effective density of states in the conduction (valence) band.

The band gap narrowing ΔE_g^{app} is modeled following [55] :

$$\Delta E_g^{\text{app}}(N_A) = 0.014 * \ln\left(\frac{N_A}{1.4 * 10^{17}}\right), \quad (3)$$

Regarding the carrier transport mechanisms, drift-diffusion is considered for homo-interfaces (c-Si/c-Si and a-Si:H/a-Si:H) and thermoionic emission together with tunneling are considered for hetero-interfaces (a-Si:H/c-Si).

3.4.2 Simulation results and discussion

The solar cell performance parameters extracted from numerical simulation are plotted in Fig. 9 as a function of the interface defect density. It is worth noting that these results were obtained for a front emitter configuration, however we found identical results (within less than 1%) in the rear emitter configuration (provided one changes the (n) a-Si:H thickness in order to keep the same short circuit current).

While the short circuit current density is almost the same for SHJ and HHJ cells (less than 0.05 mA cm⁻² difference) one can see the advantage of HHJ cells in the open-circuit voltage at high D_{it} and in the fill factor.

For D_{it} above 10⁹ cm⁻², the HHJ cell has a higher V_{OC} value than the SHJ cell. This was evidenced to originate directly from a better field effect passivation that can hinder recombination through interface defects [23]. For D_{it} below 10⁹ cm⁻² recombination at the emitter hetero-interface is no longer the limiting recombination path and does not limit the solar cell performance. This is why both SHJ and HHJ cells reach the same V_{OC} value and further reduction of D_{it} does not improve the solar cell performance.

Regarding the fill factor, an improvement is observed for the HHJ cell in the whole D_{it} range. The gain compared to SHJ cells is of 0.8% abs for D_{it} values below 5 × 10⁹ cm⁻² and slightly less at higher D_{it} . This gain can be explained, at least partially, by the better field effect passivation. Indeed, field effect improves the minority carrier lifetime at low and medium injection levels, lower than at 1-sun illumination

(here below 10¹⁶ cm⁻³) [40]. Such improvement can be shown on the simulated lifetime curves of symmetrical SHJ and HHJ precursors shown in Fig. 10, which exhibit the same trends as observed experimentally (Figs. 3 and 4). The carrier lifetime for voltages lower than V_{OC} and around the maximum power point of the IV curve is higher in the HHJ cell. As a result, a higher proportion of carriers is collected, thus enhancing the FF [41]. Such effect is also confirmed by the improvement in the pFF values experimentally observed in HHJ cells compared to the SHJ ones.

Simulations can also help explaining the decrease of both the sheet resistance (from TLM measurements on cells precursors) and the series resistance (from IV measurements on the cells) between the HHJ and SHJ cells. Indeed, as can be seen in Fig. 11, in the HHJ cell the Fermi level lies closer to the valence band in both c-Si and a-Si:H regions due to the insertion of the (p⁺) c-Si region. Therefore, the hole sheet density in c-Si is larger, explaining the lower sheet resistance observed in Fig. 6. Moreover, the larger hole concentration in a-Si:H also decreases the a-Si:H layers resistivity [16].

To quantify the contribution of the change in band bending to the FF decrease, we used the numerical simulations to calculate the resistance of both (i) a-Si:H and (p) a-Si:H layers under illumination at the maximum power point; we focus on the a-Si:H layers since they are by far the most resistive one [16]. As expected from the band diagram of Fig. 11, the calculated resistances in the a-Si:H layers are lower for the HHJ cell, 0.43 Ω cm² for the sum of both (i) and (p) a-Si:H layers, compared to 0.56 Ω cm² for the SHJ cell. The series resistance of the cell, $R_{S \text{ Cell}}$, is also lower for the HHJ cell while the FF value is larger. However the decrease in $R_{S \text{ Cell}}$ is more pronounced, suggesting that the resistance of the a-Si:H layers cannot solely explain the decrease in $R_{S \text{ Cell}}$ and the increase of FF from the SHJ to the HHJ cell (Table 3).

This is confirmed by the numerical results obtained on the SHJ_{adjusted} cell, where we only increased the a-Si:H mobility so as to adjust the a-Si:H resistance at the same level as in the HHJ cell (0.43 Ω cm²). Indeed, for this cell we observe a decrease of $R_{S \text{ Cell}}$ and an increase of FF compared to the SHJ cell, but the values are still a bit behind those of the HHJ cell, suggesting that transport across the interface through thermoionic effect is also favoured in the HHJ cell and contributes to the increase in FF.

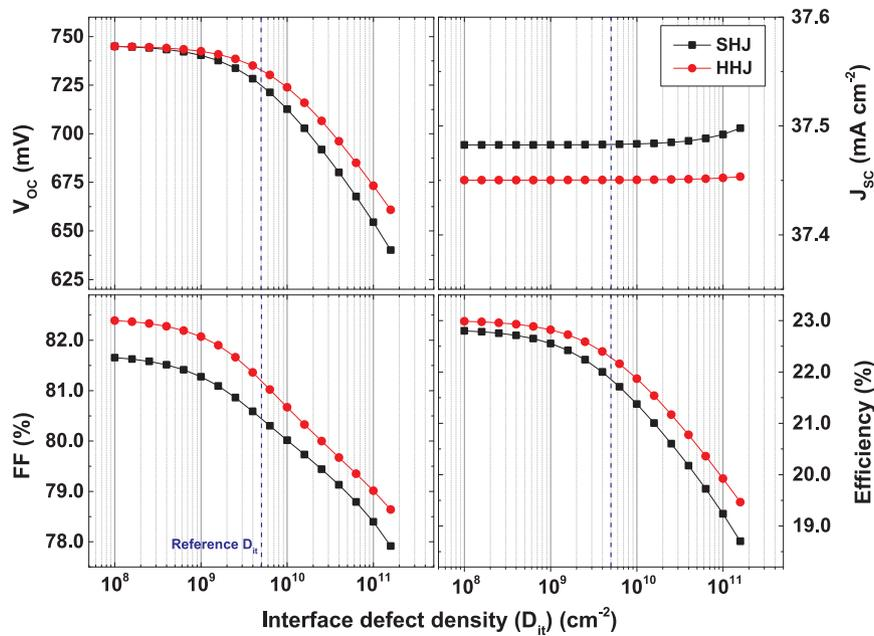


Fig. 9. Simulated SHJ and HHJ solar cells performance, open-circuit voltage (V_{oc}), short circuit current density (J_{sc}), fill factor (FF) and efficiency as a function of interface defect density (D_{it}) at the emitter side. The vertical blue dashed line marks the reference D_{it} considered for both the SHJ and HHJ cells.

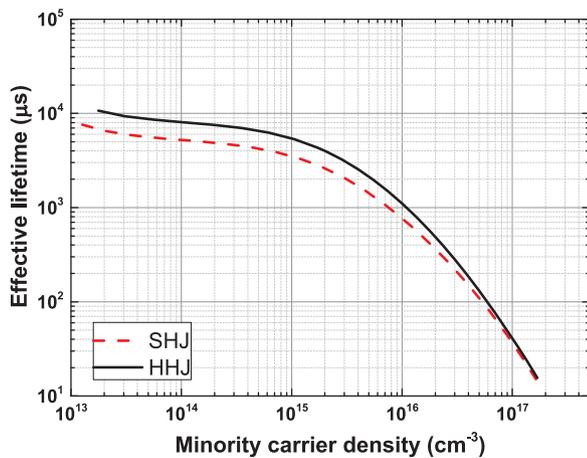


Fig. 10. Simulated injection dependent lifetime curves for HHJ and SHJ cells (plain lines and dashed lines, respectively).

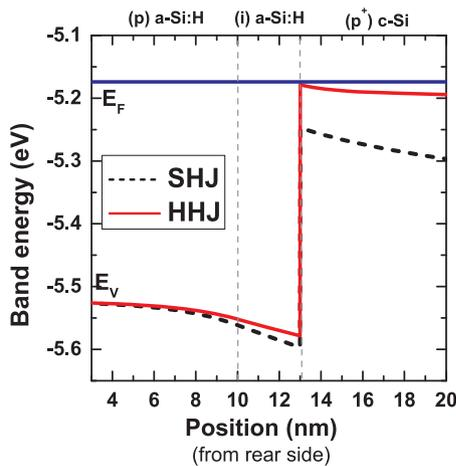


Fig. 11. Equilibrium valence band diagrams of the SHJ and HHJ cells around the hetero-interface.

Table 3

Photovoltaic parameters (open-circuit voltage, short circuit current density, fill factor and efficiency) and resistances extracted from simulations. $R_{a-Si:H}$ is the resistance of the emitter a-Si:H layers, at the maximum power point under illumination, $R_{S cell}$ is the series resistances of the cell. Values are shown for the three simulated cells: SHJ, HHJ and SHJ_{adjusted}, for which the a-Si:H mobility has been adjusted so as to have the same $R_{a-Si:H}$ value as in the HHJ cell.

	Unit	SHJ	SHJ _{adjusted}	HHJ
V_{oc}	mV	725	725	733
J_{sc}	$mA\ cm^{-2}$	37.5	37.5	37.5
FF	%	80.4	80.9	81.2
Efficiency	%	21.9	22.0	22.3
$R_{a-Si:H}$	$\Omega\ cm^2$	0.56	0.43	0.43
$R_{S cell}$	$\Omega\ cm^2$	1.08	0.94	0.74

Note that simulation results predict that the open-circuit voltage of HHJ cells should be slightly larger than that of SHJ cells, which is not observed experimentally. This is because in the simulations the interface defect density was kept at the same value for SHJ and HHJ cells. Experimentally, although we have improved the quality of the interface compared to previous work, it is likely that our HHJ cells still have a higher defect density at the heterointerface compared to the SHJ cells, which counterbalances the expected benefit from field effect passivation on the open-circuit voltage. Finally, also note that the absolute values of extracted photovoltaic parameters are slightly different in the simulated and experimental results. Indeed, the FF and efficiency improvements predicted from numerical simulation in HHJ cells are less pronounced in the experimental results. In the simulations, we have considered a 10 nm thick layer homogeneously doped at $5 \times 10^{18}\ cm^{-3}$ corresponding to a dose of $5 \times 10^{12}\ cm^{-2}$. Experimentally, HHJ₁ and HHJ₂ homo-emitters have doses in the same order of magnitudes (0.2 and $1 \times 10^{13}\ cm^{-2}$, respectively). However, the dose is distributed over more than 100 nm. Therefore, the difference in doping profiles is likely to explain discrepancies between simulations and experiments.

4. Conclusion

The first proof of concept of homo-heterojunction (HHJ) solar cells has been demonstrated. The novel architecture contains an additional

(p^+) c-Si region at the hetero-interface emitter side of an n-type silicon heterojunction solar cell (SHJ). From lifetime measurements on symmetrical precursors, a limited (i) a-Si:H passivation on the (p^+) c-Si region has been evidenced and found to be directly related to the boron surface concentration. This phenomenon is critical for the HHJ processing since the lower chemical passivation can counter-balance the improved field effect. Nevertheless, we succeeded in taking benefit from the enhanced field effect to improve the effective carrier lifetime at low injection levels by considering lowly doped (p^+) c-Si regions. This allowed us to produce n-type HHJ large area solar cells with FF and efficiencies slightly surpassing that of regular SHJ cells. From both experiments and numerical simulations, the FF improvement has been correlated to the field effect enhancement but also to the series resistance decrease arising from the modified band bending at the hetero-interface.

Although we have observed efficiency improvements with the HHJ architecture as compared to the SHJ one, these are the very first results obtained for HHJ solar cells so there is space for further improvements in order to maximize the homo-heterojunction benefits. For instance, there are many optimizations to be done concerning boron profiles management or a-Si:H layers properties tuning. The issue of annealing damages on the substrates should also be addressed to maximize the HHJ cells efficiency while decreasing its costs before evaluating the architecture potential to decrease the price of electricity.

Acknowledgements

The authors would like to acknowledge the French Environment and Energy Management Agency (ADEME) for funding this work. The authors thank the support of J. Le Perchec and P. Mur from CEA-LETI.

References

- [1] K. Masuko, M. Shigematsu, T. Hashiguchi, D. Fujishima, M. Kai, N. Yoshimura, T. Yamaguchi, Y. Ichihashi, T. Mishima, N. Matsubara, T. Yamanishi, T. Takahama, M. Taguchi, R. Maruyama, S. Okamoto, Achievement of more than 25% conversion efficiency with crystalline silicon heterojunction solar cell, *IEEE J. Photovolt.* 4 (2014) 1433–1435, <http://dx.doi.org/10.1109/JPHOTOV.2014.2352151>.
- [2] J.B. Heng, J. Fu, B. Kong, Y. Chae, W. Wang, Z. Xie, A. Reddy, K. Lam, C. Beitel, C. Liao, C. Erben, Z. Huang, Z. Xu, > 23.1% High efficiency tunnel oxide junction bifacial solar cell with electroplated Cu gridlines, in: Proceedings of the 29th European Photovoltaic Solar Energy Conference and Exhibition, Amsterdam, The Netherlands, 2014, pp. 492–496, <http://dx.doi.org/10.4229/EUPVSEC.20142014-2CO.1.2>.
- [3] T. Kinoshita, D. Fujishima, A. Yano, A. Ogane, S. Tohoda, K. Matsuyama, Y. Nakamura, N. Tokuoka, H. Kanno, H. Sakata, M. Taguchi, E. Maruyama, The approaches for high efficiency HIT solar cell with very thin (< 100 μm) silicon wafer over 23%, in: Proceedings of the 26th European Photovoltaic Solar Energy Conference and Exhibition, Hamburg, Germany, 2011, pp. 871–874, <http://dx.doi.org/10.4229/26thEUPVSEC.2011-2AO.2.6>.
- [4] J.L. Hernández, K. Yoshikawa, A. Feltrin, N. Menou, N. Valckx, E. Van Assche, D. Schroos, K. Vandersmissen, H. Philippsen, J. Poortmans, High efficiency silver-free heterojunction silicon solar cell, *Jpn. J. Appl. Phys.* 51 (2012) 10NA04, <http://dx.doi.org/10.1143/JJAP.51.10NA04>.
- [5] D. Bätzner, Y. Andraut, L. Andreetta, A. Buechel, W. Frammelsberger, C. Guerin, N. Holm, D. Lachenal, J. Meixenberger, P. Papet, B. Rau, B. Strahm, G. Wahli, F. Wuensch, Characterisation of over 21% efficient silicon heterojunction cells developed at Roth & Rau Switzerland, in: Proceedings of the 26th European Photovoltaic Solar Energy Conference and Exhibition, Hamburg, Germany, 2011, pp. 1073–1075, <http://dx.doi.org/10.4229/26thEUPVSEC.2011-2CO.14.6>.
- [6] A. Descoedres, L. Barraud, S. De Wolf, B. Strahm, D. Lachenal, C. Guérin, Z.C. Holman, F. Zicarelli, B. Demaurex, J. Seif, J. Holovsky, C. Ballif, Improved amorphous/crystalline silicon interface passivation by hydrogen plasma treatment, *Appl. Phys. Lett.* 99 (2011) 123506, <http://dx.doi.org/10.1063/1.3641899>.
- [7] D. Muñoz, T. Desrues, A.-S. Ozanne, N. Nguyen, S. de Vecchi, F. Souche, S. Martin de Nicolàs, C. Denis, P.-J. Ribeyron, Progress on high efficiency standard and interdigitated back contact silicon heterojunction solar cells, in: Proceedings of the 26th European Photovoltaic Solar Energy Conference and Exhibition, Hamburg, Germany, 2011, pp. 861–864, <http://dx.doi.org/10.4229/26thEUPVSEC.2011-2AO.2.3>.
- [8] D. Adachi, J.L. Hernández, K. Yamamoto, Impact of carrier recombination on fill factor for large area heterojunction crystalline silicon solar cell with 25.1% efficiency, *Appl. Phys. Lett.* 107 (2015) 233506, <http://dx.doi.org/10.1063/1.4937224>.
- [9] K. Yoshikawa, H. Kawasaki, W. Yoshida, T. Irie, K. Konishi, K. Nakano, T. Uto, D. Adachi, M. Kanematsu, H. Uzu, K. Yamamoto, Silicon heterojunction solar cell with interdigitated back contacts for a photoconversion efficiency over 26%, *Nature, Energy* 2 (2017) 17032, <http://dx.doi.org/10.1038/nenergy.2017.32> (<http://www.nature.com/natureenergy>).
- [10] K. Yamamoto, D. Adachi, K. Yoshikawa, W. Yoshida, T. Irie, K. Konishi, T. Fujimoto, H. Kawasaki, M. Kanematsu, H. Ishibashi, T. Uto, Y. Takahashi, T. Terashita, G. Koizumi, N. Nakanishi, M. Yoshimi, Record-Breaking Efficiency Back-Contact Heterojunction Crystalline Si Solar Cell and Module, in: Proceedings of the 33rd European Photovoltaic Solar Energy Conference and Exhibition, Amsterdam, 2017, pp. 201 – 204, doi: 10.4229/EUPVSEC.20172017-2BP.1.1.
- [11] S. De Wolf, A. Descoedres, Z.C. Holman, C. Ballif, High-efficiency silicon heterojunction solar cells: a review, *Green* 2 (2012) 7–24, <http://dx.doi.org/10.1515/green-2011-0018>.
- [12] M. Schmidt, L. Korte, A. Laades, R. Stangl, Ch Schubert, H. Angermann, E. Conrad, K. Maydell, Physical aspects of a-Si: h/c-si hetero-junction solar cells, *Thin Solid Films* 515 (2007) 7475–7480, <http://dx.doi.org/10.1016/j.tsf.2006.11.087>.
- [13] H. Angermann, T.F. Schulze, E. Conrad, J. Rappich, L. Korte, M. Schmidt, Cleaning and passivation of structured n-type si substrates: preparation and interface properties of a-Si:H/c-si hetero solar cells, in: Proceedings of the 23rd European Photovoltaic Solar Energy Conference and Exhibition, Valencia, Spain, 2008, pp. 1422–1426, <http://dx.doi.org/10.4229/23rdEUPVSEC.2008-2CV.4.31>.
- [14] Liu Jian, Huang Shihua, He Lü, Simulation of a high-efficiency silicon-based heterojunction solar cell, *J. Semicond.* 36 (2015) 044010, <http://dx.doi.org/10.1088/1674-4926/36/4/044010>.
- [15] R. Varache, O.N. Aguila, A. Valla, N. Nguyen, D. Muñoz, Role of the front electron collector in rear emitter silicon heterojunction solar cells, *IEEE J. Photovolt.* 5 (2015) 711–717, <http://dx.doi.org/10.1109/JPHOTOV.2015.2400226>.
- [16] R. Lachaume, W. Favre, P. Scheiblin, X. Garros, N. Nguyen, J. Coignus, D. Munoz, G. Reimbold, Influence of a-Si: h/i interface properties on performance of heterojunction solar cells, *Energy Procedia* 38 (2013) 770–776, <http://dx.doi.org/10.1016/j.egypro.2013.07.345>.
- [17] F. Wang, X. Zhang, L. Wang, Y. Jiang, C. Wei, S. Xu, Y. Zhao, Improved amorphous/crystalline silicon interface passivation for heterojunction solar cells by low-temperature chemical vapor deposition and post-annealing treatment, *Phys. Chem. Chem. Phys.* 16 (2014) 20202–20208, <http://dx.doi.org/10.1039/C4CP02212B>.
- [18] L. Serenelli, R. Chierchia, M. Izzi, M. Tucci, L. Martini, D. Caputo, R. Asquini, G. de Cesare, Hydrogen plasma and thermal annealing treatments on a-Si:H thin film for c-Si surface passivation, *Energy Procedia* 60 (2014) 102–108, <http://dx.doi.org/10.1016/j.egypro.2014.12.350>.
- [19] A. Florakis, T. Janssens, J. Poortmans, W. Vandervorst, Process modeling for doped regions formation on high efficiency crystalline silicon solar cells, *J. Comput. Electron.* 13 (2014) 95–107, <http://dx.doi.org/10.1007/s10825-013-0487-2>.
- [20] R. Janssen, A. Janotta, D. Dimova-Malinovska, M. Stutzmann, Optical and electrical properties of doped amorphous silicon suboxides, *Phys. Rev. B* 60 (1999) 13561–13572, <http://dx.doi.org/10.1103/physrevb.60.13561>.
- [21] M. Mews, M. Liehhaber, B. Rech, L. Korte, Valence band alignment and hole transport in amorphous/crystalline silicon heterojunction solar cells, *Appl. Phys. Lett.* 107 (2015) 013902, <http://dx.doi.org/10.1063/1.4926402>.
- [22] T. Mueller, J. Wong, A.G. Aberle, Heterojunction silicon wafer solar cells using amorphous silicon suboxides for interface passivation, *Energy Procedia* 15 (2012) 97–106, <http://dx.doi.org/10.1016/j.egypro.2012.02.012>.
- [23] T. Carrere, R. Varache, D. Muñoz, J.P. Kleider, Insertion of a thin highly doped crystalline layer in silicon heterojunction solar cells: simulation and perspectives towards a highly efficient cell concept, *J. Renew. Sustain. Energy* 7 (2015) 011202, <http://dx.doi.org/10.1063/1.4908189>.
- [24] S. Zhong, X. Hua, W. Shen, Simulation of high-efficiency crystalline silicon solar cells with homo-hetero junctions, *IEEE Trans. Electron Devices* 60 (2013) 2104–2110, <http://dx.doi.org/10.1109/TED.2013.2259830>.
- [25] M. Mikolášek, P. Přibytňý, D. Donoval, J. Marek, A. Chvála, M. Molnár, J. Kováč, Suppression of interface recombination by buffer layer for back contacted silicon heterojunction solar cells, *Appl. Surf. Sci.* 312 (2014) 145–151, <http://dx.doi.org/10.1016/j.apsusc.2014.05.110>.
- [26] B. Demaurex, (2014). Passivating contacts for homojunction solar cells using a-Si:H/c-Si hetero-interfaces, Thèse École polytechnique fédérale de Lausanne EPFL, no. 6392. <http://dx.doi.org/10.5075/epfl-thesis-6392>.
- [27] Yu-Hsien Lin, Yung-Chun Wu, Hsin-Chiang You, Chun-Hao Chen, Ping-Hua Chen, Yi-He Tsai, Yi-Yun Yang, K.S. Chang-Liao, Silicon heterojunction solar cells using AlOx and plasma-immersion ion implantation, *Energies* 7 (2014) 3653–3663, <http://dx.doi.org/10.3390/en7063653>.
- [28] T. Carrere, R. Varache, J. Le Perchec, C. Denis, D. Muñoz, J.-P. Kleider, Silicon bulk issues during processing of homo-heterojunction solar cells, *Energy Procedia* 77 (2015) 451–457, <http://dx.doi.org/10.1016/j.egypro.2015.07.064>.
- [29] F. Jay F, Nouveaux substrats de silicium cristallin destinés aux cellules photovoltaïques à haut rendement : cas du silicium mono-like et du dopage aux donneurs thermiques liés à l'oxygène pour les cellules à hétérojonction de silicium, thèse de l'Université Grenoble Alpes, NNT:2016GREAI010, 2016.
- [30] A. Lanterne, S. Gall, Y. Veschetti, R. Cabal, M. Coig, F. Milési, A. Tauzin, High efficiency fully implanted and co-annealed bifacial n-type solar cells, *Energy Procedia* 38 (2013) 283–288, <http://dx.doi.org/10.1016/j.egypro.2013.07.279>.
- [31] B. Hoex, J.J.H. Gielis, M.C.M. van de Sanden, W.M.M. Kessels, On the c-Si surface passivation mechanism by the negative-charge-dielectric Al₂O₃, *J. Appl. Phys.* 104 (2008) 113703, <http://dx.doi.org/10.1063/1.3021091>.
- [32] R.A. Sinton, A. Cuevas, Contactless determination of current-voltage characteristics and minority-carrier lifetimes in semiconductors from quasi-steady-state photo-conductance data, *Appl. Phys. Lett.* 69 (1996) 2510–2512, <http://dx.doi.org/10.1063/1.117723>.

- [33] S. Bowden, V. Yelundur, A. Rohatgi, Implied- V_{oc} and Suns- V_{oc} measurements in multicrystalline solar cells, in: Proceedings of the 29th IEEE Photovoltaic Specialists Conference (PVSC), New Orleans, Louisiana, 2002, pp. 371–374, <<http://dx.doi.org/10.1109/PVSC.2002.1190536>>.
- [34] D.L. Meier, D.K. Schroder, Contact resistance: its measurement and relative importance to power loss in a solar cell, IEEE Trans. Electron Devices 31 (1984) 647–653, <<http://dx.doi.org/10.1109/T-ED.1984.21584>>.
- [35] L.K. Mak, C.M. Rogers, D.C. Northrop, Specific contact resistance measurements on semiconductors, J. Phys. E: Sci. Instrum. 22 (1989) 317–321, <<http://dx.doi.org/10.1088/0022-3735/22/5/010>>.
- [36] E. Rimini, Ion Implantation: basics to device fabrication, The Springer International Series in Engineering and Computer Science 293 Springer, 1995, <<http://dx.doi.org/10.1007/978-1-4615-2259-1>>.
- [37] S. Harrison, A. Danel, C. Roux, D. Heslinga, F. Ozanne, D. Muñoz, P.J. Ribeyron, CEA-INES Heterojunction Solar Cell LabFab Industrial Pilot Line: Production Capability Demonstration, Roadmap to 22% Mean Efficiency, in: Proceedings of the 29th European Photovoltaic Solar Energy Conference and Exhibition, Amsterdam, The Netherlands, pp. 1049–1052, <<http://dx.doi.org/10.4229/EUPVSEC.20142014-2AV.3.33>>, 2014.
- [38] M. Bivour, M. Reusch, S. Schroer, F. Feldmann, J. Temmler, H. Steinkemper, M. Hermle, Doped layer optimization for silicon heterojunctions by injection-level-dependent open-circuit voltage measurements, IEEE J. Photovolt. 4 (2014) 566–574, <<http://dx.doi.org/10.1109/JPHOTOV.2013.2294757>>.
- [39] T. Trupke, R.A. Bardos, M.D. Abbott, P. Würfel, E. Pink, Y. Augarten, F.W. Chen, K. Fisher, J.E. Cotter, M. Kasemann, M. Rüdiger, S. Kontermann, M.C. Schubert, M. The, S.W. Glunz, W. Warta, D. Macdonald, J. Tan, A. Cuevas, J. Bauer, R. Gupta, O. Breitenstein, G. Tarnowski, H.P. Hartmann, D.H. Neuhaus, J.M. Fernandez, Progress with luminescence imaging for the characterisation of silicon wafers and solar cells, in: Proceedings of the 22nd European Photovoltaic Solar Energy Conference and Exhibition, Milan, Italy, 2007, pp. 22–31.
- [40] D. Pysch, A. Mette, S.W. Glunz, A review and comparison of different methods to determine the series resistance of solar cells (6 November), Sol. Energy Mater. Sol. Cells 91 (18) (2007) 1698–1706.
- [41] S.W. Glunz, D. Biro, S. Rein, W. Warta, Field-effect passivation of the SiO_2 Si interface, J. Appl. Phys. 86 (1999) 683–691, <<http://dx.doi.org/10.1063/1.370784>>.
- [42] A. Descoedres, Z.C. Holman, L. Barraud, S. Morel, B. Demareux, J. Geissbühler, J. P. Seif, S. De Wolf, C. Ballif, Silicon heterojunction solar cells on n-and p-type wafers with efficiencies above 20%, in: Proceedings of the 27th European Photovoltaic Solar Energy Conference and Exhibition, Frankfurt, Germany, 2012, pp. 647–51, <<http://dx.doi.org/10.4229/27thEUPVSEC.2012-2BO.6.2>>.
- [43] F. Jay, J. Veirman, N. Najid, D. Muñoz, S. Dubois, A. Jouini, Exclusively thermal donor-doped Cz wafers for silicon heterojunction solar cell technology, Energy Procedia 55 (2014) 533–538, <<http://dx.doi.org/10.1016/j.egypro.2014.08.020>>.
- [44] H.J. Stein, S.K. Hahn, S.C. Shatas, Rapid thermal annealing and regrowth of thermal donors in silicon, J. Appl. Phys. 59 (1986) 3495–3502, <<http://dx.doi.org/10.1063/1.336820>>.
- [45] M. Tomassini, J. Veirman, R. Varache, E. Letty, S. Dubois, Y. Hu, Ø. Nielsen, Recombination activity associated with thermal donor generation in monocrystalline silicon and effect on the conversion efficiency of heterojunction solar cells, J. Appl. Phys. 119 (2016) 084508, <<http://dx.doi.org/10.1063/1.4942212>>.
- [46] J. Bullock, D. Yan, Y. Wan, A. Cuevas, B. Demareux, A. Hessler-Wyser, S. De Wolf, Amorphous silicon passivated contacts for diffused junction silicon solar cells, J. Appl. Phys. 115 (2014) 163703, <<http://dx.doi.org/10.1063/1.4872262>>.
- [47] K. Carstens, M. Dahlinger, E. Hoffmann, J.R. Köhler, R. Zapf-Gottwick, J.H. Werner, Universal passivation for p++ and n++ areas on IBC solar cells, Energy Procedia 77 (2015) 779–785, <<http://dx.doi.org/10.1016/j.egypro.2015.07.110>>.
- [48] J.P. Kleider, A.S. Gudovskikh, P. Roca i Cabarrocas, Determination of the conduction band offset between hydrogenated amorphous silicon and crystalline silicon from surface inversion layer conductance measurements, Appl. Phys. Lett. 92 (2008) 162101, <<http://dx.doi.org/10.1063/1.2907695>>.
- [49] N.D. Arora, J.R. Hauser, D.J. Roulston, Electron and hole mobilities in silicon as a function of concentration and temperature, IEEE Trans. Electron Devices ED 29 (1982) 292–295, <<http://dx.doi.org/10.1109/T-ED.1982.20698>>.
- [50] R. Varache, J.P. Kleider, M.E. Gueunier-Farret, L. Korte, Silicon heterojunction solar cells: optimization of emitter and contact properties from analytical calculation and numerical simulation, Mater. Sci. Eng. B 178 (2013) 593–598, <<http://dx.doi.org/10.1016/j.mseb.2012.11.011>>.
- [51] M. Powell, S. Deane, Defect-pool model and the hydrogen density of states in hydrogenated amorphous silicon, Phys. Rev. B 53 (1996) 10121–10132, <<http://dx.doi.org/10.1103/PhysRevB.53.10121>>.
- [52] J.G. Fossum, R.P. Mertens, D.S. Lee, J.F. Nijs, Carrier recombination and lifetime in highly doped silicon, Solid-State Electron. 26 (1983) 569–576, <[http://dx.doi.org/10.1016/0038-1101\(83\)90173-9](http://dx.doi.org/10.1016/0038-1101(83)90173-9)>.
- [53] S. Bellone, G. Busatto, C.M. Ransom, Recombination measurement of n-type heavily doped layer in high/low silicon junctions, IEEE Trans. Electron Devices ED 38 (1991) 532–537, <<http://dx.doi.org/10.1109/16.75163>>.
- [54] S.M. Sze, Physics of Semiconductor Devices, 2nd ed., Wiley, 1998.
- [55] A. Cuevas, P.A. Basore, G. Giroult-Matlakowski, C. Dubois, Surface recombination velocity of highly doped n-type silicon, J. Appl. Phys. 80 (1996) 3370–3375, <<http://dx.doi.org/10.1063/1.363250>>.